

# Experimental Determination of the Interaction Potential between a Helium Atom and the Interior Surface of a C<sub>60</sub> Fullerene Molecule

George Razvan Bacanu,<sup>1</sup> Tanzeeha Jafari,<sup>2</sup> Mohamed Aouane,<sup>3</sup> Jyrki Rantaharju,<sup>1</sup> Mark Walkey,<sup>1</sup> Gabriela Hoffman,<sup>1</sup> Anna Shugai,<sup>2</sup> Urmas Nagel,<sup>2</sup> Monica Jiménez-Ruiz,<sup>3</sup> Anthony J. Horsewill,<sup>4</sup> Stéphane Rols,<sup>3</sup> Toomas Rõõm,<sup>2</sup> Richard J. Whitby,<sup>1</sup> and Malcolm H. Levitt<sup>1</sup>

<sup>1</sup>*School of Chemistry, University of Southampton, Southampton, SO17 1BJ, UK*

<sup>2</sup>*National Institute of Chemical Physics and Biophysics, Tallinn, 12618, Estonia*

<sup>3</sup>*Institut Laue-Langevin, BP 156, 38042 Grenoble, France*

<sup>4</sup>*School of Physics and Astronomy, University of Nottingham, Nottingham, NG7 2RD*

(\*Electronic mail: mhl@soton.ac.uk)

(Dated: 17 September 2021)

The interactions between atoms and molecules may be described by a potential energy function of the nuclear coordinates. Non-bonded interactions between neutral atoms or molecules are dominated by repulsive forces at short range and attractive dispersion forces at medium range. Experimental data on the detailed interaction potentials for non-bonded interatomic and intermolecular forces is scarce. Here we use terahertz spectroscopy and inelastic neutron scattering to determine the potential energy function for the non-bonded interaction between single He atoms and encapsulating C<sub>60</sub> fullerene cages, in the helium endofullerenes <sup>3</sup>He@C<sub>60</sub> and <sup>4</sup>He@C<sub>60</sub>, synthesised by molecular surgery techniques. The experimentally derived potential is compared to estimates from quantum chemistry calculations, and from sums of empirical two-body potentials.

## I. INTRODUCTION

Non-bonded intermolecular interactions determine the structure and properties of most forms of matter. The *potential energy function* specifies the dependence of the potential energy on the nuclear coordinates of the interacting moieties, within the Born-Oppenheimer approximation<sup>1</sup>. The estimation of potential functions for non-bonded interactions remains an active research area of computational chemistry<sup>2-4</sup>. *Ab initio* methods are capable of high accuracy but are usually too computationally expensive to be applied to anything but very small molecular systems. Computational techniques with good scaling properties such as density functional theory (DFT) are generally imprecise for non-bonded interactions, unless customised adjustments are made<sup>3-5</sup>. The accuracy of quantum chemistry algorithms is often assessed by seeking convergence with respect to the calculation level, or number of basis functions<sup>2</sup>.

Advances in all fields of science require comparison with experiment. Unfortunately, detailed experimental data on intermolecular potential energy surfaces is scarce. Some information may be gained by comparing crystal structures and energetics with those derived from model potentials<sup>6</sup>. The equilibrium structures, dissociation energies and vibrational frequencies of intermolecular complexes and clusters may be studied in the gas phase and molecular beams<sup>7-12</sup>. However these measurements encounter difficulties with control of the local sample temperature, and only provide information on potential minima, and their local properties close to potential minima (unless tunnelling splittings are resolved). Atomic beam diffraction may also provide information<sup>13-15</sup>.

An ideal set of systems for the study of intermolecular interactions is provided by atomic and molecular endofullerenes, in which single atoms or small molecules are encapsulated in closed carbon cages<sup>16-19</sup>. A range of small-molecule endofullerenes is available in macroscopic quantities through the

multi-step synthetic route known as “molecular surgery”<sup>20</sup>, including H<sub>2</sub>@C<sub>60</sub><sup>18</sup>, H<sub>2</sub>@C<sub>70</sub><sup>21</sup>, H<sub>2</sub>O@C<sub>60</sub><sup>19</sup>, HF@C<sub>60</sub><sup>22</sup>, CH<sub>4</sub>@C<sub>60</sub><sup>23</sup>, and their isotopologues. Endofullerenes containing noble gas atoms, and containing two encapsulated species, may also be produced<sup>21,24-30</sup>. Endofullerenes are chemically very stable, may be prepared in a pure and homogeneous solid form, and may be studied at almost any desired temperature.

At low temperatures, the translational modes (and for non-monatomic species, the internal degrees of freedom) of the endohedral species are quantized. The quantum levels may be probed by a wide range of spectroscopic techniques<sup>31</sup>, including infrared spectroscopy<sup>22,32-36</sup>, pulsed terahertz spectroscopy<sup>37</sup>, nuclear magnetic resonance<sup>22,29,34,38-40</sup>, and inelastic neutron scattering<sup>22,34,41,42</sup>. When performed at cryogenic temperatures, these techniques reveal a rich energy level structure for the quantized modes of the encapsulated systems<sup>22,32,34,41,43</sup>. The quantum structure has been studied in detail using models of the confining potential, sometimes combined with cage-induced modifications of the rotational and vibrational characteristics of the guest molecule<sup>32,33,35,36,43-56</sup>.

There are two main ways to describe the interaction potential between the encapsulated species and the cage. One approach describes the interaction potential as a sum over many two-body Lennard-Jones functions involving each endohedral atom and all 60 carbon atoms of the cage<sup>44-46,49,50,52,53,55,56</sup>, sometimes introducing “additional sites” on the endohedral species as well<sup>46,52,53</sup>. One disadvantage of this approach is that the summed potential has an undesirable dependence on the precise radius of the encapsulating fullerene cage. An alternative approach, which we call “model-free”, describes the interaction potential as a sum of orthogonal spatial functions<sup>32,33,35,36,43,47,48</sup>. The latter approach makes no assumptions about the cage geometry and is better-suited for a comparison with computational chemistry methods.

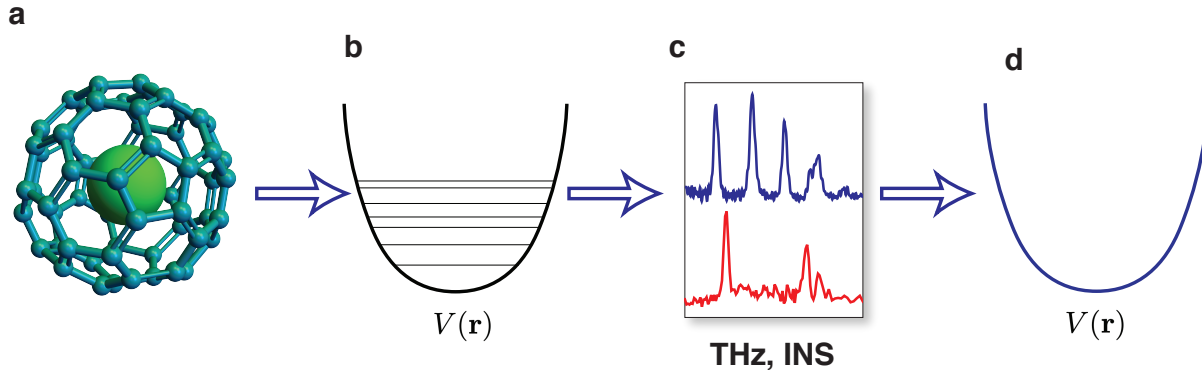


FIG. 1. **(a)** A  $C_{60}$  cage encapsulates a single noble gas atom. **(b)** The confinement potential of the encapsulated atom is described by the function  $V(\mathbf{r})$ . The quantum energy levels and wavefunctions of the encapsulated atom depend on  $V(\mathbf{r})$ . **(c)** Transitions between the energy levels are detected in the bulk solid state at low temperature by terahertz spectroscopy and inelastic neutron scattering. **(d)** Analysis of the spectroscopic and neutron scattering data allows determination of the potential energy function, which may be compared with computational chemistry estimates.

In this report, we “go back to basics” by studying the simplest atomic endofullerene,  $\text{He}@C_{60}$ , consisting of  $C_{60}$  fullerene cages each encapsulating a single helium atom (figure 1a). Terahertz and neutron scattering data is acquired and fitted by a simple quantum-mechanical model consisting of a particle confined by a three-dimensional potential well. This allows us to define a “model-free” atom-fullerene potential, with no assumptions about whether it may be expressed as the sum of many two-body interactions.

Although  $\text{He}@C_{60}$  was first made in trace amounts by gas-phase methods<sup>16,17,57</sup>, molecular surgery techniques now provide both isotopologues  $^3\text{He}@C_{60}$  and  $^4\text{He}@C_{60}$  in high purity and macroscopic quantities<sup>25,30</sup>. These synthetic advances have made it feasible to perform terahertz spectroscopy and inelastic neutron scattering experiments on solid polycrystalline samples of  $\text{He}@C_{60}$  at low temperature, with good signal-to-noise ratio.

At first sight,  $\text{He}@C_{60}$  is an unpromising object of study by both terahertz spectroscopy and neutron scattering. Since He atoms are neutral, their translational motion is not expected to interact with electromagnetic radiation. Furthermore, both  $^3\text{He}$  and  $^4\text{He}$  isotopes have small neutron scattering cross-sections, and  $^3\text{He}$  is a strong neutron absorber. Fortunately, although these concerns are valid, they are not fatal. An off-centre He atom acquires a small induced electric dipole through its interactions with the encapsulating  $C_{60}$  cage, as is known for  $\text{H}_2@C_{60}$ <sup>32</sup>. The induced dipole is approximately linearly dependent on the displacement from the cage centre, allowing the He atom to interact weakly with THz irradiation. The feeble neutron scattering of both He isotopes may be compensated by a sufficiently large sample quantity.

We compare the experimentally determined potential to estimates from empirical two-body interaction potentials, and from quantum chemistry calculations. Empirical two-body potentials give widely divergent results, even when those po-

tentials are based on experimental helium-graphite scattering data. Møller-Plesset perturbation theory techniques and density functional theory (DFT) methods which explicitly include, or are empirically corrected to account for, dispersive interactions, are shown to provide good estimates for the interaction potential.

## II. MATERIALS AND METHODS

### A. Sample Preparation

$^3\text{He}@C_{60}$  and  $^4\text{He}@C_{60}$  were synthesised using a solid-state process for the critical step, as described in reference 30. The initial filling factors were 30% to 50%. The samples were further purified by recirculating HPLC on Cosmosil Buckyprep columns to remove trace impurities of  $\text{H}_2\text{O}@C_{60}$ . Without this precaution, strong neutron scattering by the hydrogen nuclei interferes strongly with the INS measurements. For THz spectroscopy samples of high filling factor were required to get sufficient signal and were prepared by further extensive recirculating HPLC. All samples were sublimed under vacuum before spectroscopic measurements.

### B. Terahertz Spectroscopy

THz absorption spectra were measured with an interferometer using a mercury arc light source and a 4 K bolometer as an intensity detector. The typical instrumental resolution was  $0.3 \text{ cm}^{-1}$ , which is below the width of the measured THz absorption lines. The  $^4\text{He}@C_{60}$  sample had a filling factor of  $f = 88.2 \pm 0.5\%$  while the  $^3\text{He}@C_{60}$  had a filling factor of  $f = 97.2 \pm 0.5\%$ , as determined by  $^{13}\text{C}$  NMR. The sample

pellets were pressed from fine powders of solid He@C<sub>60</sub>. The temperature dependence of the absorption spectra was measured by using a variable-temperature optical cryostat. More information is in the Supplementary Material.

### C. Inelastic Neutron Scattering

INS experiments were conducted using the IN1-Lagrange spectrometer at the Institut Laue-Langevin (ILL) in Grenoble. Incident neutrons are provided by the “hot source” moderator of the reactor, resulting in a high flux neutron beam. A choice of three different single crystal monochromators, namely Si(111), Si(311) and Cu(220) are used to define the incident energy of the monochromatic neutron beam arriving at the sample using Bragg reflection. The neutrons scattered by the interaction with the sample enter a secondary spectrometer comprising a large area array of pyrolytic graphite analyzer crystals. The focussing geometry of the secondary spectrometer ensures that only neutrons with a fixed kinetic energy of 4.5 meV are detected by the <sup>3</sup>He detector. INS spectra were recorded in the energy transfer range [5, 200] meV for the <sup>3</sup>He@C<sub>60</sub> sample, while it was reduced to [5, 60] meV for <sup>4</sup>He@C<sub>60</sub> as the time allowed for performing the latter experiment was reduced.

The powdered samples, with respective mass of 1067 mg for <sup>3</sup>He@C<sub>60</sub> ( $f = 45\%$ ) and 294 mg for <sup>4</sup>He@C<sub>60</sub> ( $f = 40\%$ ) were loaded inside an Al foil and further inserted inside a cylindrical annulus before they were mounted at the tip of an orange cryostat and placed inside the IN1 spectrometer beam. The sample temperature was kept around 2.7 K. In order to subtract background and scattering from Al and from the C<sub>60</sub> cage, a blank mass matching sample of C<sub>60</sub> was measured using the same setup and an empty cell was also measured. In order to account for the strong absorption of <sup>3</sup>He@C<sub>60</sub>, a Cd sample was also measured enabling to correct from the incident energy dependent absorption of the sample. The neutron counts in figure 3 were normalized to the incident neutron flux.

## III. EXPERIMENTAL RESULTS

### A. Terahertz spectroscopy

Terahertz absorption spectra for <sup>3</sup>He@C<sub>60</sub> and <sup>4</sup>He@C<sub>60</sub> at two different temperatures are shown in figure 2. For both isotopologues, the high-temperature spectrum displays a comb of several clearly resolved THz peaks, with the <sup>3</sup>He peaks having higher frequencies than those of <sup>4</sup>He. As discussed below, the combs of THz peaks indicate that the potential energy function  $V(r)$  for the encapsulated He does not have a purely quadratic dependence on the displacement  $r$  of the He atom from the cage centre. This indicates that the He dynamics is not well-described as a harmonic three-dimensional oscillator.

The 5 K spectra in figure 2 display a single peak with partially-resolved fine structure, for both <sup>3</sup>He@C<sub>60</sub> and

<sup>4</sup>He@C<sub>60</sub>. These fundamental peaks correspond to transitions from the quantum ground states of He in the two isotopologues. The fine structure requires further investigation, but may be associated with a small perturbation of the confining potential by the merohedral disorder in the crystal lattice, meaning the inhomogeneous orientations of neighbouring C<sub>60</sub> cages with respect to each other. Similar effects have been identified for H<sub>2</sub>@C<sub>60</sub><sup>42</sup>.

### B. Inelastic neutron scattering

Inelastic neutron scattering spectra for <sup>3</sup>He@C<sub>60</sub> and <sup>4</sup>He@C<sub>60</sub> are shown in figure 3. The figure shows the difference between the INS of the He endofullerenes and that

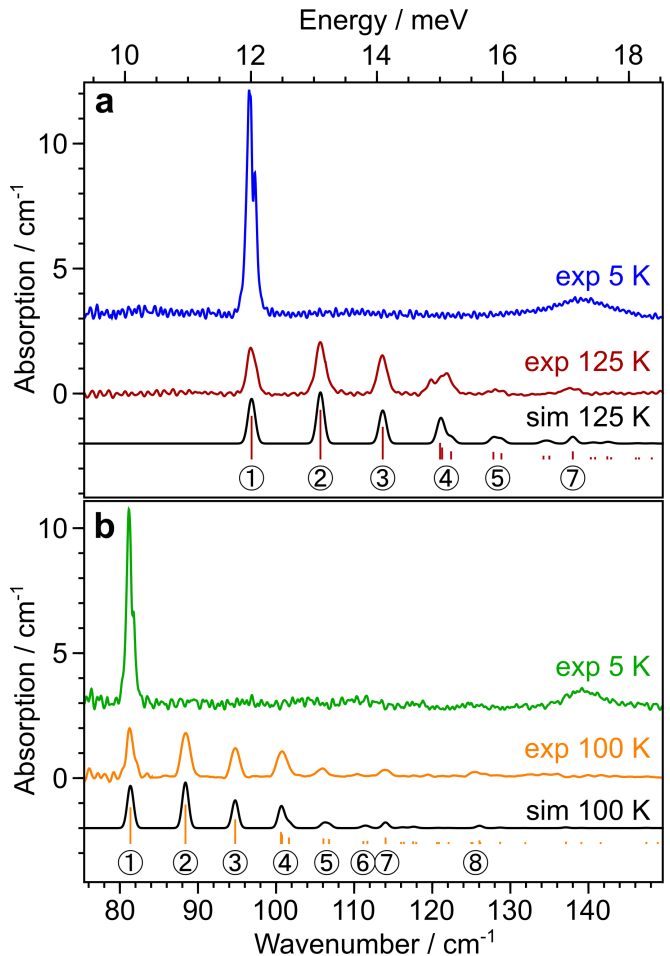


FIG. 2. THz spectroscopy of He endofullerenes. (a) THz absorption spectra of <sup>3</sup>He@C<sub>60</sub> at temperatures of 5 K (blue) and 125 K (red). (b) THz absorption spectra of <sup>4</sup>He@C<sub>60</sub> at temperatures of 5 K (green) and 100 K (orange). In both cases, the short vertical bars indicate the predicted positions of the terahertz absorption peaks for the radial potential energy function specified in table I, and their height is proportional to the absorption area. In both cases the black curve is the sum of gaussian peaks with position and area defined by the vertical bars. The THz peaks are numbered according to the transition assignments in figure 4(b).

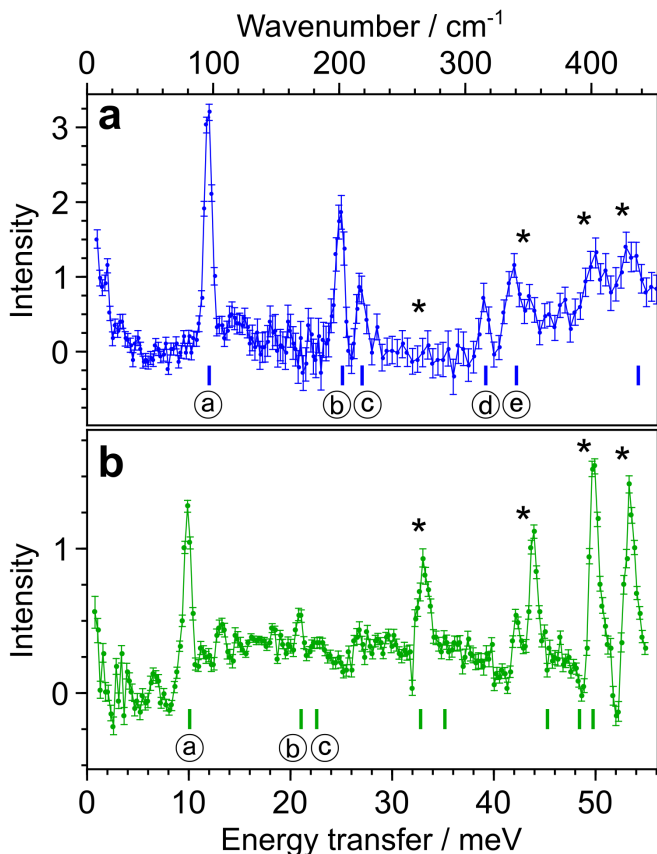


FIG. 3. Inelastic neutron scattering of He endofullerenes. **(a)** Inelastic neutron scattering spectra of  ${}^3\text{He}@C_{60}$  at a temperature of 2.7 K (blue). **(b)** Inelastic neutron scattering spectra of  ${}^4\text{He}@C_{60}$  at a temperature of 2.7 K (green). In both cases, a weighted difference between the scattering of He@C<sub>60</sub> and pure C<sub>60</sub> is shown, with the weighting factors adjusted for best subtraction of the C<sub>60</sub> background. The short vertical bars indicate the predicted positions of the INS peaks for the quantized He motion under the radial potential energy function specified in table I. The INS peaks are labelled according to the transition assignments in figure 4(b). The peaks above  $\sim 250\text{ cm}^{-1}$  and marked by asterisks are due to scattering from the C<sub>60</sub> cages, whose modes are slightly modified in frequency by the presence of endohedral He.

of pure C<sub>60</sub>. The INS spectra before subtraction are shown in the Supplementary Material. Since C<sub>60</sub> has no vibrational modes below  $\sim 250\text{ cm}^{-1}$ , and the low-energy phonon spectrum cancels precisely for the empty and filled fullerenes, the peaks below this energy threshold are clearly attributable to the quantized modes of the confined He atoms. As in the case of THz spectroscopy, the  ${}^3\text{He}$  INS peaks are at higher energies than for  ${}^4\text{He}$ .

The strong features above  $\sim 250\text{ cm}^{-1}$  are attributed to the known vibrational modes of C<sub>60</sub> molecules<sup>58</sup>. Raman studies have shown that the radial vibrational modes of the C<sub>60</sub> cages are slightly blue-shifted by the presence of an endohedral noble gas atom<sup>59</sup>. These shifts lead to imperfect cancellation in the INS difference spectra, causing the dispersion-like features in figure 3 which are marked by asterisks. These

subtraction artefacts are much stronger for  ${}^4\text{He}$  than for  ${}^3\text{He}$ , for two reasons: (i) the C<sub>60</sub> vibrational modes are slightly more shifted for  ${}^4\text{He}$  than for  ${}^3\text{He}$ , due to its larger mass; (ii)  ${}^4\text{He}$  has a much lower scattering cross-section than  ${}^3\text{He}$ . The poor signal-to-noise ratio for  ${}^4\text{He}$  causes some of the expected peaks to be barely visible, an example being the peak marked “c” in figure 3(b).

## IV. ANALYSIS

### A. Energy levels and transitions

The Schrödinger equation for the confined atom (within the Born-Oppenheimer approximation), is given by

$$\hat{H}(\mathbf{r})\psi_{\mathbf{q}}(\mathbf{r}) = E_{\mathbf{q}}\psi_{\mathbf{q}}(\mathbf{r}) \quad (1)$$

where  $\mathbf{q}$  describes a set of quantum numbers,  $\mathbf{q} = \{q_1, q_2, \dots\}$ , and  $E_{\mathbf{q}}$  is the energy of the stationary quantum state. The Hamiltonian operator  $\hat{H}$  is given by

$$\hat{H}(\mathbf{r}) = -\frac{\hat{p}^2}{2M} + V(\mathbf{r}) \quad (2)$$

where  $\hat{p}$  is the momentum operator and  $M$  is the atomic mass. In general, the energy levels  $E_{\mathbf{q}}$  and stationary state wavefunctions  $\psi_{\mathbf{q}}$  depend strongly on the potential energy function  $V(\mathbf{r})$ , where  $\mathbf{r}$  represents the nuclear coordinates of the encapsulated atom (figure 1b).

Equations 1 and 2 assume that the cage coordinates are fixed, and neglect environmental effects from beyond the cage – although the treatment may readily be extended to include the electrostatic influence of the lattice environment, as has been done for studies of H<sub>2</sub>O@C<sub>60</sub><sup>36,51,55,56</sup>.

The potential energy of the He atom inside the cage may be described by a potential function  $V(r, \theta, \phi)$ , where  $r$  is the displacement of the He nucleus from the cage centre, and  $(\theta, \phi)$  are polar angles. The C<sub>60</sub> cage has icosahedral symmetry, but may be treated as spherical to a good approximation, at low excitation energies of the endohedral atom. The angular dependence may be dropped by assuming approximate spherical symmetry,  $V(r, \theta, \phi) \simeq V(r)$ . We assume a radial potential energy function of the form  $V(r) = V_2r^2 + V_4r^4 + V_6r^6$  where  $\{V_2, V_4, V_6\}$  are polynomial coefficients.

The energy eigenvalues and eigenstates are given by  $E_{nlm}$  and  $\psi_{nlm}(r, \theta, \phi)$  respectively. The principal quantum number  $n$  takes values  $n \in \{0, 1, \dots\}$  with the angular momentum quantum number  $\ell$  given by  $\ell \in \{0, 2, \dots, n\}$  (for even  $n$ ) and  $\ell \in \{1, 3, \dots, n\}$  (for odd  $n$ )<sup>60</sup>. The azimuthal quantum number takes values  $m \in \{-\ell, -\ell+1, \dots, \ell\}$ . For spherical symmetry, the energies are independent of  $m$ , so the energy level  $E_{nl}$  is  $(2\ell+1)$ -fold degenerate. The icosahedral cage symmetry introduces perturbation terms of spherical rank 6 and higher, and only breaks the degeneracies of spherical states with large angular momentum quantum numbers. Within the spherical approximation, the stationary quantum states  $\psi_{nlm}(r, \theta, \phi)$  are given by products of radial functions  $R_{nl}(r)$  and spherical harmonics  $Y_{\ell m}(\theta, \phi)$ , just as for the electronic orbitals of a hydrogen atom<sup>60</sup>.

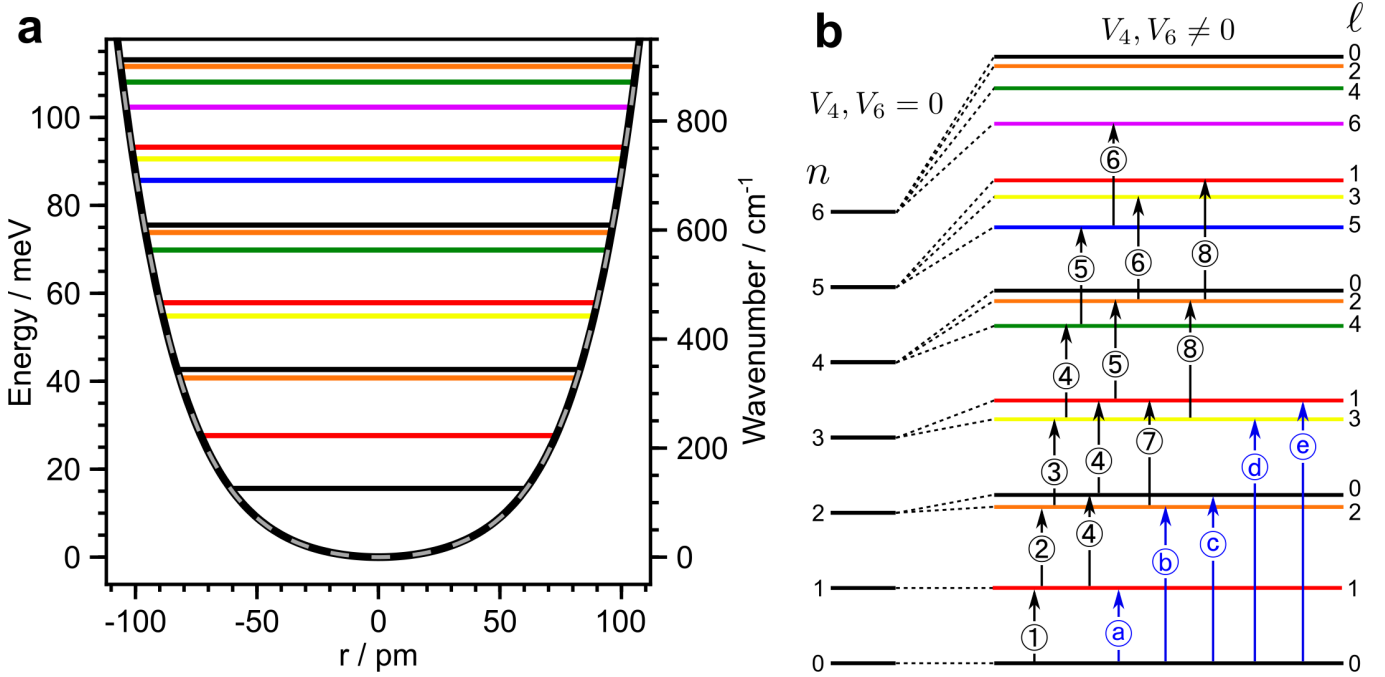


FIG. 4. (a) The radial potential energy functions  $V(r)$  for  $^3\text{He}$  in  $\text{C}_{60}$  (solid black curve) and for  $^4\text{He}$  in  $\text{C}_{60}$  (dashed grey curve), together with the quantized energy levels for  $^3\text{He}$ . The  $^3\text{He}$  and  $^4\text{He}$  potential curves are superposed within this energy range, leading to a “railway track” appearance of the plotted curve. The best-fit polynomial coefficients are given in table I. (b) Energy levels of the confined  $^3\text{He}$  atoms, labelled by the quantum numbers  $n\ell$ . The energy levels for a harmonic oscillator are shown on the left. The finite  $V_4$  and  $V_6$  terms break the degeneracies between terms with different  $\ell$ . All levels are  $(2\ell + 1)$ -fold degenerate. The transitions observed in THz spectroscopy are labelled by circled numbers in black, and correspond to the peaks in figure 2. The transitions observed in INS are labelled by circled letters in blue, and correspond to the peaks in figure 3. Colours are used to indicate the  $\ell$  values of the energy levels.

The eigenvalues and eigenstates depend on the potential coefficients  $\{V_2, V_4, V_6\}$  and the mass of the He atom. The electric-dipole-allowed transitions, which are observed in THz spectroscopy and described by the induced dipole moment coefficient  $A_1$ , have the selection rule  $\Delta\ell = \pm 1$ , see Supplementary Material. There are no relevant selection rules for the neutron scattering peaks.

## B. Fitting of the Potential

We treat the  $V_4$  and  $V_6$  terms as perturbations of the quadratic  $V_2$  term, which corresponds to an isotropic three-dimensional harmonic oscillator. The solutions of the Schrödinger equation for the isotropic 3D harmonic oscillator are well-known<sup>60,61</sup>, and are given by:

$$|n\ell m\rangle(r, \theta, \phi) = R_{n\ell}(r)Y_{\ell m}(\theta, \phi), \quad (3)$$

where the principal quantum number is given by  $n \in \{0, 1, 2, \dots\}$  and the angular momentum quantum number  $\ell$  takes values  $\{0, 2, \dots, n\}$  for even  $n$ , and  $\{1, 3, \dots, n\}$  for odd  $n$ . The radial wavefunctions  $R_{n\ell}(r)$  are proportional to generalised Laguerre polynomials<sup>62,63</sup>, while the angular parts  $Y_{\ell m}$  are spherical harmonics. The energy eigenvalues are given by

$$E_{n\ell m} = \hbar\omega_0\left(n + \frac{3}{2}\right) \quad (4)$$

with the fundamental vibrational frequency  $\omega_0 = (2V_2/\mu)^{1/2}$ , where  $\mu$  is the reduced mass (assumed here to be equal to the mass of the  $^3\text{He}$  or  $^4\text{He}$  atom, since each  $\text{C}_{60}$  molecule is more than two orders of magnitude more massive than the encapsulated atom, and is also coupled to the lattice).

The Schrödinger equation was solved approximately for finite  $V_4$  and  $V_6$  by numerically diagonalizing a matrix with elements given by  $\langle n\ell m|V_4r^4 + V_6r^6|n'\ell'm'\rangle$ . Since the assumed Hamiltonian retains isotropic symmetry, all matrix elements are independent of the quantum number  $m$  and vanish for  $\ell \neq \ell'$  and  $m \neq m'$ . In practice the matrix was bounded by quantum numbers  $n \leq 18$ , after checking for convergence. The THz peak intensities and peak positions were fitted, as described in the Supplementary Material, allowing numerical estimation of the potential parameters  $V_2$  (or  $\omega_0$ ),  $V_4$  and  $V_6$ , and the induced dipole moment amplitude  $A_1$ . The derived eigenvalues were used to estimate the INS peak positions.

The fitting of the potential was performed independently for the two He isotopes. The best fit solutions for the potential coefficients, and their confidence limits, are given in table I.

Figure 4(a) shows the best-fit potential functions for  $^3\text{He}$  and  $^4\text{He}$  inside the interior cavity of  $\text{C}_{60}$ . The best-fit potential has a distinct U-shape which deviates strongly from the parabolic form of a harmonic oscillator. The best-fit potential curves  $^3\text{He}$  and  $^4\text{He}$  differ by not more than  $\pm 1 \text{ cm}^{-1}$  over the plotted energy range.

An energy level diagram for the confined He atoms, marked

TABLE I. Best fit polynomial coefficients and confidence limits for the radial potential function  $V(r) = V_2 r^2 + V_4 r^4 + V_6 r^6$  and induced dipole function  $d_{1q} = \sqrt{4\pi/3} A_1 r Y_{1q}(\theta, \phi)$  experienced by the confined He isotopes, see Supplementary Material.

Parameter	${}^3\text{He}$	${}^4\text{He}$
$V_2 / \text{meV pm}^{-2}$	$(2.58 \pm 0.06) 10^{-3}$	$(2.50 \pm 0.05) 10^{-3}$
$V_4 / \text{meV pm}^{-4}$	$(3.37 \pm 0.15) 10^{-7}$	$(3.61 \pm 0.11) 10^{-7}$
$V_6 / \text{meV pm}^{-6}$	$(2.79 \pm 0.12) 10^{-11}$	$(2.63 \pm 0.09) 10^{-11}$
$A_1 / \text{D pm}^{-1}$	$(4.38 \pm 0.09) 10^{-4}$	$(4.58 \pm 0.06) 10^{-4}$

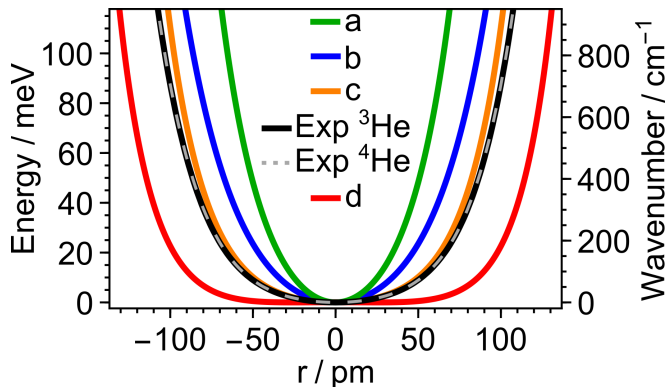


FIG. 5. Comparison of the experimentally determined radial potentials  $V(r)$  ( ${}^3\text{He}$ : solid black curve;  ${}^4\text{He}$ : dashed grey curve, superposed on the  ${}^3\text{He}$  curve to give a “train track” appearance) with sums of reported He...C interaction potentials: (a, green) Lennard-Jones 6-8-12 potential with parameters from Carlos *et al.*<sup>14</sup>; (b, blue) Modified Buckingham potential (implemented in the MM3 program, as reported by Jiménez-Vázquez *et al.*<sup>64</sup>); (c, orange) Lennard-Jones 6-12 potential with parameters from Pang and Brisse<sup>65</sup>; (d, red) Lennard-Jones 6-12 potential with parameters from Carlos *et al.*<sup>14</sup>. The potentials used in (a) and (d) were used for the fitting of He...C scattering data<sup>14</sup>. The functional forms of the potentials and their associated parameters are given in the Supplementary Material. In all cases the He atom was displaced from the cage centre towards the nucleus of a carbon atom. The confidence limits in the structural data for  $\text{C}_{60}$ <sup>66</sup> lead to error margins on the empirical curves which are smaller than the plotted linewidths.

with the observed transitions, is shown in figure 4(b). The predicted positions of the relevant THz and INS transitions are shown by the vertical bars in figures 2 and 3. Although some of the higher-energy transitions in the INS data are partially obscured by  $\text{C}_{60}$  features, the agreement with the spectroscopic results is gratifying. The remaining discrepancies between experiment and theory are minor, such as the form of the peak labelled 4 in figure 2(a), and are currently unexplained. The close correspondence of the derived potential curves for  ${}^3\text{He}$  and  ${}^4\text{He}$ , despite the different masses of the isotopes and the very different observed frequencies, attests to the validity of the determination of  $V(r)$ .

### C. Comparison with Empirical Potentials

There have been numerous attempts to model the non-bonded interactions between atoms using empirical two-body potential functions such as the Lennard-Jones (LJ) 6-12 potential, or by more complex functional forms. Suitable functions and parameters have been proposed for the He...C interaction<sup>14,15,64,65,67</sup>. Some of the proposed two-body potentials were developed for modelling the scattering of He atoms from a graphite surface<sup>14,15</sup>.

Figure 5 compares the experimental  $V(r)$  curve with predictions from published He...C two-body interaction functions. In each case, the total potential energy  $V(r)$  was estimated by locating the He atom a distance  $r$  along a line from the centre of the cage towards a C atom, and summing the contributions from all 60 two-body He...C potentials. The direction of the He displacement has a negligible effect on the calculated potential curves over the relevant energy range (see Supplementary Material). The derived potentials are very sensitive to the geometry of the  $\text{C}_{60}$  cage, especially its radius  $R$ . We fixed the locations of all C nuclei to the best current estimates from neutron diffraction<sup>66</sup>, as follows: Bond lengths  $h = 138.14 \pm 0.27$  pm for C-C bonds shared by two hexagons,  $p = 145.97 \pm 0.18$  pm for C-C bonds shared by a hexagon and a pentagon, and distance of all carbon atoms from the cage centre  $R = 354.7 \pm 0.5$  pm. The width of the curves in figure 5 is greater than their confidence limits, which are dominated by the uncertainties in the structural parameters. Explicit functional forms and parameters for the empirical two-body potentials are given in the Supplementary Material.

The most striking feature of Figure 5 is the wide variation of derived potentials for different two-body interaction models. Of all the proposed two-body potentials, the Lennard-Jones 6-12 potential with parameters given by Pang and Brisse<sup>65</sup> (curve c) provides the best agreement with experiment. The isotropic two-body potentials derived by fitting experimental He/graphite scattering data<sup>14,15</sup> (curves a and d) give poor fits to the experimental He@ $\text{C}_{60}$  potential.

### D. Comparison with Quantum Chemistry

The He@ $\text{C}_{60}$  system is too large to be treated at the full *ab initio* level of quantum chemistry. The availability of an experimental radial potential function  $V(r)$  allows the direct evaluation of approximate computational chemistry techniques – not only at the equilibrium geometry, but also for displacements of the He atom from the centre of the  $\text{C}_{60}$  cage.

The radial potential  $V(r)$  was evaluated by estimating the energy of a He@ $\text{C}_{60}$  system using a range of computational chemistry algorithms, with the He atom displaced by  $r$  from the centre of the  $\text{C}_{60}$  cage. In all cases the locations of the carbon atoms were fixed to the  $\text{C}_{60}$  geometry as determined by neutron diffraction<sup>66</sup>, with the same parameters as used for the evaluation of the empirical potentials. The He was moved on the line connecting the cage centre to a carbon nucleus. The direction of the He displacement has a negligible effect on the predicted potential curves over the relevant en-

ergy range (see Supplementary Material). The potentials were calculated using the Psi4 program<sup>68</sup>. The functionals used for DFT were: (i) the B3LYP functional, which is one of the most popular semi-empirical hybrid functionals<sup>69–73</sup>; (ii) the B3LYP functional including the Grimme D3 empirical dispersion correction with Beck-Johnson damping<sup>5,74</sup>; (iii) the  $\omega$ B97X-V functional, which includes a contribution from the non-local VV10 correlation functional and is designed to handle non-covalent interactions<sup>69</sup>. The potential was also calculated using second-order Møller-Plesset perturbation (MP2) theory<sup>2</sup> including empirical spin-component-scaling factors (SCS)<sup>75</sup>. All potential calculations employed a counterpoise basis-set-superposition-error correction, and converged to a good approximation with the correlation-consistent cc-pVXZ (X=D, T, Q, 5) basis sets<sup>76,77</sup>. The calculations with  $X = Q$  and  $X = 5$  were found to agree within 1% in the case of MP2 theory and within 7% for the two DFT-functionals. More details on the quantum chemistry calculations are given in the Supplementary Material.

Some comparisons are shown in Figure 6. Density functional theory with the popular B3LYP functional<sup>69–73</sup> overestimates the steepness of the confining potential, although the correspondence with experiment is improved by including the empirical D3 correction with Beck-Johnson damping<sup>5,74</sup>. DFT with the  $\omega$ B97X-V functional<sup>69</sup>, and Møller-Plesset perturbation (MP2) theory with spin-component-scaling factors (SCS)<sup>75</sup>, both give an acceptable correspondence between the calculated and experimentally determined potentials.

## V. DISCUSSION

We have showed that the quantized energy levels of helium atoms encapsulated in  $C_{60}$  cages may be probed by THz spectroscopy and INS, despite the weak interactions of the He atoms with the electromagnetic field and with neutrons. The spectroscopic features were analysed to obtain a detailed potential energy function for the interaction between the encapsulated species and the surrounding cage – an interaction dominated by non-bonded dispersion forces which are hard to estimate experimentally. An excellent correspondence was obtained between the interaction potentials derived from independent  ${}^3\text{He}@C_{60}$  and  ${}^4\text{He}@C_{60}$  measurements, despite the different peak positions for the two samples.

The experimental  $V(r)$  curve was compared with sums of published two-body  $\text{He}\cdots\text{C}$  interactions. With few exceptions the summed two-body potentials have a poor correspondence with the experimental result. It is not a great surprise that the interaction of a He atom with a highly delocalized electronic structure such as  $C_{60}$  is hard to model as the sum of individual atom-atom interactions.

We also compared the experimentally derived interaction potential with those derived by quantum chemistry techniques. This allowed the validation of DFT methods which have been developed to deal with dispersive interactions, including the popular B3LYP functional with the D3 empirical dispersion correction<sup>5,74</sup>, and the  $\omega$ B97X-V functional which incorporates the non-local VV10 correlation functional

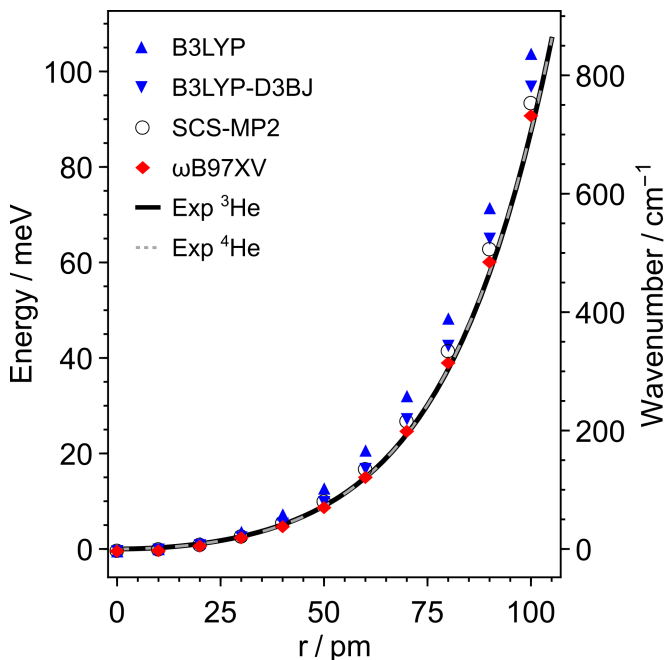


FIG. 6. Comparison of the experimentally determined  $\text{He}@C_{60}$  radial potentials  $V(r)$  ( ${}^3\text{He}$ : solid black curve;  ${}^4\text{He}$ : dashed grey curve, superposed on the  ${}^3\text{He}$  curve) with quantum chemical calculations using density functional and Møller-Plesset perturbation theories<sup>2</sup>, as follows: ( $\blacktriangle$ ) DFT using the B3LYP functional<sup>70–73</sup>; ( $\blacktriangledown$ ) DFT using the B3LYP functional with D3BJ correction<sup>5,74</sup>; ( $\blacklozenge$ ) DFT using the  $\omega$ B97XV functional<sup>69,78</sup>; ( $\circ$ ) Spin-component-scaled Møller-Plesset perturbation theory (SCS-MP2).<sup>75</sup>

and has been parameterised using a training set rich in non-bonding interactions<sup>69</sup>. Møller-Plesset perturbation theory with spin-component-scaling factors<sup>75</sup> also provides a good description of the confining potential of the encapsulated He atoms.

There are small discrepancies between the calculated and observed potentials. However it is not yet known whether the remaining discrepancies reflect the limitations in the quantum chemistry algorithms, or the limitations in the assumptions made when interpreting the experimental data – for example, the neglect of the influence exerted by the encapsulated He atoms on the cage radius. Precise measurements of the  $\text{He}@C_{60}$  cage geometry by neutron scattering or X-ray diffraction are planned.

He atoms are small, have no static dipole moment, and a low polarizability. This makes  $\text{He}@C_{60}$  a relatively easy case for computational chemistry. A stiffer challenge for computational chemistry is likely to be presented by compounds in which the endohedral species is polar, such as  $\text{H}_2\text{O}@C_{60}$ <sup>24</sup> and  $\text{HF}@C_{60}$ <sup>22</sup>, and by endofullerenes such as  $\text{CH}_4@C_{60}$ <sup>23</sup>, where the fit with the cage is much tighter. Furthermore, the study of systems with multiple atoms or molecules encapsulated in the same fullerene cage<sup>24,26,27</sup> should allow the study of non-bonded molecule-molecule and molecule-atom interactions.

## SUPPLEMENTAL MATERIAL

The supplemental material includes: technical details of the terahertz spectroscopy; technical details of the inelastic neutron scattering measurements; quantum theory of a confined atom in a spherical potential, including fitting procedures for the confining potential; details of the two-body potentials; technical details of the computational chemistry calculations.

## AUTHOR CONTRIBUTIONS

G.R.B. conceived the THz experiments. M.W., G.H. and R.J.W. synthesised and purified the compounds. G.R.B., T.J., A.S., U.N. and T.R. performed the THz experiments and processed the THz data. A.J.H. and S.R. designed the INS experiments. G.R.B., M.A. and S.R. performed the INS experiments and processed the INS data. G.R.B., M.A. and T.R. derived the potential function. J.R. and R.J.W. performed the quantum chemistry calculations. G.R.B., M.A., J.R., A.J.H., S.R., T.R., R.J.W. and M.H.L. developed the concept and drafted the paper. All authors reviewed the manuscript.

## ACKNOWLEDGMENTS

This research was supported by EPSRC-UK (grant numbers EP/P009980/1, EP/T004320/1 and EP/P030491/1), the Estonian Ministry of Education and Research institutional research funding IUT23-3, personal research funding PRG736, the European Regional Development Fund project TK134, and the European Union's Horizon 2020 research and innovation programme under the Marie Skłodowska-Curie grant agreement No 891400. The Institut Laue-Langevin is acknowledged for providing neutron beam time, and support for M.A. through the ILL PhD program. The authors acknowledge the use of the IRIDIS High Performance Computing Facility, and associated support services at the University of Southampton, in the completion of this work.

## DATA AVAILABILITY STATEMENT

The data that support the findings of this study are available from the corresponding author upon reasonable request.

<sup>1</sup>D. Wales, *Energy Landscapes: Applications to Clusters, Biomolecules and Glasses*, Cambridge Molecular Science (Cambridge University Press, Cambridge, 2004).

<sup>2</sup>F. Jensen, *Introduction to Computational Chemistry*, 3rd ed. (Wiley, Chichester, 2017).

<sup>3</sup>M. Waller and S. Grimme, "Weak Intermolecular Interactions: A Supermolecular Approach," in *Handbook of Computational Chemistry*, edited by J. Leszczynski (Springer Netherlands, Dordrecht, 2016) pp. 1–27.

<sup>4</sup>Y. Shao, Z. Gan, E. Epifanovsky, A. T. B. Gilbert, M. Wormit, J. Kussmann, A. W. Lange, A. Behn, J. Deng, X. Feng, D. Ghosh, M. Goldey, P. R. Horn, L. D. Jacobson, I. Kaliman, R. Z. Khaliullin, T. Kuš, A. Landau, J. Liu, E. I. Proynov, Y. M. Rhee, R. M. Richard, M. A. Rohrdanz, R. P. Steele, E. J. Sundstrom, H. L. W. III, P. M. Zimmerman, D. Zuev, B. Albrecht, E. Alguire, B. Austin, G. J. O. Beran, Y. A. Bernard, E. Berquist,

K. Brandhorst, K. B. Bravaya, S. T. Brown, D. Casanova, C.-M. Chang, Y. Chen, S. H. Chien, K. D. Closser, D. L. Crittenden, M. Diedenhofen, R. A. D. Jr, H. Do, A. D. Dutoi, R. G. Edgar, S. Fatehi, L. Fusti-Molnar, A. Ghysels, A. Golubeva-Zadorozhnaya, J. Gomes, M. W. D. Hanson-Heine, P. H. P. Harbach, A. W. Hauser, E. G. Hohenstein, Z. C. Holden, T.-C. Jagau, H. Ji, B. Kaduk, K. Khistyayev, J. Kim, J. Kim, R. A. King, P. Klunzinger, D. Kosenkov, T. Kowalczyk, C. M. Krauter, K. U. Lao, A. D. Laurent, K. V. Lawler, S. V. Levchenko, C. Y. Lin, F. Liu, E. Livshits, R. C. Lochan, A. Luenser, P. Manohar, S. F. Manzer, S.-P. Mao, N. Mardirossian, A. V. Marenich, S. A. Maurer, N. J. Mayhall, E. Neuscamman, C. M. Oana, R. Olivares-Amaya, D. P. O'Neill, J. A. Parkhill, T. M. Perrine, R. Peverati, A. Prociuk, D. R. Rehn, E. Rosta, N. J. Russ, S. M. Sharada, S. Sharma, D. W. Small, A. Sodt, T. Stein, D. Stück, Y.-C. Su, A. J. W. Thom, T. Tsuchimochi, V. Vanovschi, L. Vogt, O. Vydrov, T. Wang, M. A. Watson, J. Wenzel, A. White, C. F. Williams, J. Yang, S. Yeganeh, S. R. Yost, Z.-Q. You, I. Y. Zhang, X. Zhang, Y. Zhao, B. R. Brooks, G. K. L. Chan, D. M. Chipman, C. J. Cramer, W. A. G. III, M. S. Gordon, W. J. Hehre, A. Klamt, H. F. S. III, M. W. Schmidt, C. D. Sherrill, D. G. Truhlar, A. Warshel, X. Xu, A. Aspuru-Guzik, R. Baer, A. T. Bell, N. A. Besley, J.-D. Chai, A. Dreuw, B. D. Dunietz, T. R. Furlani, S. R. Gwaltney, C.-P. Hsu, Y. Jung, J. Kong, D. S. Lambrecht, W. Liang, C. Ochsenfeld, V. A. Rassolov, L. V. Slipchenko, J. E. Subotnik, T. V. Voorhis, J. M. Herbert, A. I. Krylov, P. M. W. Gill, and M. Head-Gordon, "Advances in molecular quantum chemistry contained in the Q-Chem 4 program package," *Mol. Phys.* **113**, 184–215 (2015).

<sup>5</sup>S. Grimme, J. Antony, S. Ehrlich, and H. Krieg, "A consistent and accurate ab initio parametrization of density functional dispersion correction (DFT-D) for the 94 elements H-Pu," *J. Chem. Phys.* **132**, 154104 (2010).

<sup>6</sup>F. A. Momany, L. M. Carruthers, R. F. McGuire, and H. A. Scheraga, "Intermolecular potentials from crystal data. III. Determination of empirical potentials and application to the packing configurations and lattice energies in crystals of hydrocarbons, carboxylic acids, amines, and amides," *J. Phys. Chem.* **78**, 1595–1620 (1974).

<sup>7</sup>F. N. Keutsch and R. J. Saykally, "Water clusters: Untangling the mysteries of the liquid, one molecule at a time," *PNAS* **98**, 10533–10540 (2001).

<sup>8</sup>P. Hobza and K. Müller-Dethlefs, *Non-Covalent Interactions: Theory and Experiment* (The Royal Society of Chemistry, 2009).

<sup>9</sup>L. Zhu and P. Johnson, "Mass analyzed threshold ionization spectroscopy," *J. Chem. Phys.* **94**, 5769–5771 (1991).

<sup>10</sup>H. Krause and H. J. Neusser, "Dissociation energy of neutral and ionic benzene-noble gas dimers by pulsed field threshold ionization spectroscopy," *J. Chem. Phys.* **99**, 6278–6286 (1993).

<sup>11</sup>A. Van Orden and R. J. Saykally, "Small Carbon Clusters: Spectroscopy, Structure, and Energetics," *Chem. Rev.* **98**, 2313–2358 (1998).

<sup>12</sup>T. P. Softley, "Applications of molecular Rydberg states in chemical dynamics and spectroscopy," *Int. Rev. Phys. Chem.* **23**, 1–78 (2004).

<sup>13</sup>D. Farias and K.-H. Rieder, "Atomic beam diffraction from solid surfaces," *Rep. Prog. Phys.* **61**, 1575–1664 (1998).

<sup>14</sup>W. E. Carlos and M. W. Cole, "Interaction between a He atom and a graphite surface," *Surface Science* **91**, 339–357 (1980).

<sup>15</sup>M. W. Cole, D. R. Frankl, and D. L. Goodstein, "Probing the helium-graphite interaction," *Rev. Mod. Phys.* **53**, 199–210 (1981).

<sup>16</sup>M. Saunders, H. A. Jimenez-Vazquez, R. J. Cross, and R. J. Poreda, "Stable Compounds of Helium and Neon: He@C60 and Ne@C60," *Science* **259**, 1428–1430 (1993).

<sup>17</sup>M. Saunders, R. J. Cross, H. A. Jimenez-Vazquez, R. Shimshi, and A. Khong, "Noble Gas Atoms Inside Fullerenes," *Science* **271**, 1693–1697 (1996).

<sup>18</sup>K. Komatsu, M. Murata, and Y. Murata, "Encapsulation of Molecular Hydrogen in Fullerene C60 by Organic Synthesis," *Science* **307**, 238–240 (2005).

<sup>19</sup>K. Kurotobi and Y. Murata, "A Single Molecule of Water Encapsulated in Fullerene C60," *Science* **333**, 613–616 (2011).

<sup>20</sup>Y. Rubin, T. Jarrosson, G.-W. Wang, M. D. Bartberger, K. N. Houk, G. Schick, M. Saunders, and R. J. Cross, "Insertion of Helium and Molecular Hydrogen Through the Orifice of an Open Fullerene," *Angew. Chem. Int. Ed.* **40**, 1543–1546 (2001).

<sup>21</sup>M. Murata, S. Maeda, Y. Morinaka, Y. Murata, and K. Komatsu, "Synthesis and Reaction of Fullerene C70 Encapsulating Two Molecules of H<sub>2</sub>," *J. Am. Chem. Soc.* **130**, 15800–15801 (2008).



- <sup>22</sup>A. Krachmalnicoff, R. Bounds, S. Mamone, S. Alom, M. Concistrè, B. Meier, K. Kouřil, M. E. Light, M. R. Johnson, S. Rols, A. J. Horsewill, A. Shugai, U. Nagel, T. Rööm, M. Carravetta, M. H. Levitt, and R. J. Whitby, "The dipolar endofullerene HF@C60," *Nat Chem* **8**, 953–957 (2016).
- <sup>23</sup>S. Bloodworth, G. Sotinova, S. Alom, S. Vidal, G. R. Bacanu, S. J. Elliott, M. E. Light, J. M. Herniman, G. J. Langley, M. H. Levitt, and R. J. Whitby, "First Synthesis and Characterization of CH<sub>4</sub>@C60," *Angew. Chem. Int. Ed.* **58**, 5038–5043 (2019).
- <sup>24</sup>Y. Murata, S. Maeda, M. Murata, and K. Komatsu, "Encapsulation and Dynamic Behavior of Two H<sub>2</sub> Molecules in an Open-Cage C70," *J. Am. Chem. Soc.* **130**, 6702–6703 (2008).
- <sup>25</sup>Y. Morinaka, F. Tanabe, M. Murata, Y. Murata, and K. Komatsu, "Rational synthesis, enrichment, and 13C NMR spectra of endohedral C60 and C70 encapsulating a helium atom," *Chem. Commun.* **46**, 4532–4534 (2010).
- <sup>26</sup>R. Zhang, M. Murata, T. Aharen, A. Wakamiya, T. Shimoaka, T. Hasegawa, and Y. Murata, "Synthesis of a distinct water dimer inside fullerene C 70," *Nature Chem* **8**, 435–441 (2016).
- <sup>27</sup>R. Zhang, M. Murata, A. Wakamiya, T. Shimoaka, T. Hasegawa, and Y. Murata, "Isolation of the simplest hydrated acid," *Sci. Adv.* **3**, e1602833 (2017).
- <sup>28</sup>S. Bloodworth, G. Hoffman, M. C. Walkey, G. R. Bacanu, J. M. Herniman, M. H. Levitt, and R. J. Whitby, "Synthesis of Ar@C60 using molecular surgery," *Chem. Commun.* **56**, 10521–10524 (2020).
- <sup>29</sup>G. R. Bacanu, J. Rantaharju, G. Hoffman, M. C. Walkey, S. Bloodworth, M. Concistrè, R. J. Whitby, and M. H. Levitt, "An Internuclear J-Coupling of 3He Induced by Molecular Confinement," *J. Am. Chem. Soc.* **142**, 16926–16929 (2020).
- <sup>30</sup>G. Hoffman, M. C. Walkey, J. Gräsvik, G. R. Bacanu, S. Alom, S. Bloodworth, M. E. Light, M. H. Levitt, and R. J. Whitby, "A solid state intramolecular Wittig reaction enables efficient synthesis of endofullerenes including Ne@C60, 3He@C60 and HD@C60," *Angew. Chem. Int. Ed.* **60**, 8960–8966 (2021).
- <sup>31</sup>M. H. Levitt, "Spectroscopy of light-molecule endofullerenes," *Philos. Trans. R. Soc. Math. Phys. Eng. Sci.* **371**, 20120429 (2013).
- <sup>32</sup>S. Mamone, M. Ge, D. Huvonen, U. Nagel, A. Danquigny, F. Cuda, M. C. Gossel, Y. Murata, K. Komatsu, M. H. Levitt, T. Rööm, and M. Carravetta, "Rotor in a cage: Infrared spectroscopy of an endohedral hydrogen-fullerene complex," *J Chem Phys* **130**, 081103–4 (2009).
- <sup>33</sup>M. Ge, U. Nagel, D. Huvonen, T. Rööm, S. Mamone, M. H. Levitt, M. Carravetta, Y. Murata, K. Komatsu, X. Lei, and N. J. Turro, "Infrared spectroscopy of endohedral HD and D<sub>2</sub> in C60," *J. Chem. Phys.* **135**, 114511 (2011).
- <sup>34</sup>C. Beduz, M. Carravetta, J. Y.-C. Chen, M. Concistrè, M. Denning, M. Frunzi, A. J. Horsewill, O. G. Johannessen, R. Lawler, X. Lei, M. H. Levitt, Y. Li, S. Mamone, Y. Murata, U. Nagel, T. Nishida, J. Ollivier, S. Rols, T. Rööm, R. Sarkar, N. J. Turro, and Y. Yang, "Quantum rotation of ortho and para-water encapsulated in a fullerene cage," *Proc. Natl. Acad. Sci.* **109**, 12894–12898 (2012).
- <sup>35</sup>T. Rööm, L. Peedu, M. Ge, D. Huvonen, U. Nagel, S. Ye, M. Xu, Z. Bačić, S. Mamone, M. H. Levitt, M. Carravetta, J.-C. Chen, X. Lei, N. J. Turro, Y. Murata, and K. Komatsu, "Infrared spectroscopy of small-molecule endofullerenes," *Philos. Trans. R. Soc. Math. Phys. Eng. Sci.* **371**, 20110631 (2013).
- <sup>36</sup>A. Shugai, U. Nagel, Y. Murata, Y. Li, S. Mamone, A. Krachmalnicoff, S. Alom, R. J. Whitby, M. H. Levitt, and T. Rööm, "Infrared spectroscopy of an endohedral water in fullerene," *J. Chem. Phys.* **154**, 124311 (2021).
- <sup>37</sup>S. S. Zhukov, V. Balos, G. Hoffman, S. Alom, M. Belyanchikov, M. Nebioglu, S. Roh, A. Pronin, G. R. Bacanu, P. Abramov, M. Wolf, M. Dressel, M. H. Levitt, R. J. Whitby, B. Gorshunov, and M. Sajadi, "Rotational coherence of encapsulated ortho and para water in fullerene-C 60 revealed by time-domain terahertz spectroscopy," *Sci. Rep.* **10**, 18329 (2020).
- <sup>38</sup>N. J. Turro, J. Y. C. Chen, E. Sartori, M. Ruzzi, A. Marti, R. Lawler, S. Jockusch, J. López-Gejo, K. Komatsu, and Y. Murata, "The Spin Chemistry and Magnetic Resonance of H<sub>2</sub>@C60. From the Pauli Principle to Trapping a Long Lived Nuclear Excited Spin State inside a Buckyball," *Acc. Chem. Res.* (2009).
- <sup>39</sup>S. Mamone, M. Concistrè, I. Heinmaa, M. Carravetta, I. Kuprov, G. Wall, M. Denning, X. Lei, J. Y. C. Chen, Y. Li, Y. Murata, N. J. Turro, and M. H. Levitt, "Nuclear Magnetic Resonance of Hydrogen Molecules Trapped inside C70 Fullerene Cages," *ChemPhysChem* **14**, 3121–3130 (2013).
- <sup>40</sup>G. R. Bacanu, G. Hoffman, M. Amponsah, M. Concistrè, R. J. Whitby, and M. H. Levitt, "Fine structure in the solution state 13C-NMR spectrum of C60 and its endofullerene derivatives," *Phys. Chem. Chem. Phys.* **22**, 11850–11860 (2020).
- <sup>41</sup>A. J. Horsewill, K. S. Panesar, S. Rols, J. Ollivier, M. R. Johnson, M. Carravetta, S. Mamone, M. H. Levitt, Y. Murata, K. Komatsu, J. Y. C. Chen, J. A. Johnson, X. Lei, and N. J. Turro, "Inelastic neutron scattering investigations of the quantum molecular dynamics of a H<sub>2</sub> molecule entrapped inside a fullerene cage," *Phys. Rev. B* **85**, 205440 (2012).
- <sup>42</sup>S. Mamone, M. R. Johnson, J. Ollivier, S. Rols, M. H. Levitt, and A. J. Horsewill, "Symmetry-breaking in the H<sub>2</sub>@C60 endofullerene revealed by inelastic neutron scattering at low temperature," *Phys. Chem. Chem. Phys.* **18**, 1998–2005 (2016).
- <sup>43</sup>S. Mamone, M. Jiménez-Ruiz, M. R. Johnson, S. Rols, and A. J. Horsewill, "Experimental, theoretical and computational investigation of the inelastic neutron scattering spectrum of a homonuclear diatomic molecule in a nearly spherical trap: H<sub>2</sub>@C60," *Phys. Chem. Chem. Phys.* **18**, 29369–29380 (2016).
- <sup>44</sup>M. Xu, F. Sebastianelli, Z. Bačić, R. Lawler, and N. J. Turro, "H-2, HD, and D-2 inside C-60: Coupled translation-rotation eigenstates of the endohedral molecules from quantum five-dimensional calculations," *J. Chem. Phys.* **129**, 064313 (2008).
- <sup>45</sup>M. Xu, F. Sebastianelli, Z. Bačić, R. Lawler, and N. J. Turro, "Quantum dynamics of coupled translational and rotational motions of H[sub 2] inside C[sub 60]," *J Chem Phys* **128**, 011101–4 (2008).
- <sup>46</sup>M. Xu, F. Sebastianelli, B. R. Gibbons, Z. Bačić, R. Lawler, and N. J. Turro, "Coupled translation-rotation eigenstates of H<sub>2</sub> in C60 and C70 on the spectroscopically optimized interaction potential: Effects of cage anisotropy on the energy level structure and assignments," *J. Chem. Phys.* **130**, 224306 (2009).
- <sup>47</sup>M. Ge, U. Nagel, D. Huvonen, T. Rööm, S. Mamone, M. H. Levitt, M. Carravetta, Y. Murata, K. Komatsu, J. Y.-C. Chen, and N. J. Turro, "Interaction potential and infrared absorption of endohedral H<sub>2</sub> in C60," *J. Chem. Phys.* **134**, 054507 (2011).
- <sup>48</sup>S. Mamone, J. Y. C. Chen, R. Bhattacharyya, M. H. Levitt, R. G. Lawler, A. J. Horsewill, T. Rum, Z. Bačić, and N. J. Turro, "Theory and spectroscopy of an incarcerated quantum rotor: The infrared spectroscopy, inelastic neutron scattering and nuclear magnetic resonance of H<sub>2</sub>@C60 at cryogenic temperature," *Coord. Chem. Rev.* **255**, 938–948 (2011).
- <sup>49</sup>M. Xu, S. Ye, A. Powers, R. Lawler, N. J. Turro, and Z. Bačić, "Inelastic neutron scattering spectrum of H<sub>2</sub>@C60 and its temperature dependence decoded using rigorous quantum calculations and a new selection rule," *The Journal of Chemical Physics* **139**, 064309 (2013).
- <sup>50</sup>P. M. Felker and Z. Bačić, "Communication: Quantum six-dimensional calculations of the coupled translation-rotation eigenstates of H<sub>2</sub>O@C60," *J. Chem. Phys.* **144**, 201101 (2016).
- <sup>51</sup>P. M. Felker, V. Vlček, I. Hietanen, S. FitzGerald, D. Neuhauser, and Z. Bačić, "Explaining the symmetry breaking observed in the endofullerenes H<sub>2</sub>@C60, HF@C60, and H<sub>2</sub>O@C60," *Phys. Chem. Chem. Phys.* **19**, 31274–31283 (2017).
- <sup>52</sup>Z. Bačić, "Perspective: Accurate treatment of the quantum dynamics of light molecules inside fullerene cages: Translation-rotation states, spectroscopy, and symmetry breaking," *The Journal of Chemical Physics* **149**, 100901 (2018).
- <sup>53</sup>Z. Bačić, M. Xu, and P. M. Felker, "Coupled Translation–Rotation Dynamics of H<sub>2</sub> and H<sub>2</sub>O Inside C60 : Rigorous Quantum Treatment," in *Advances in Chemical Physics* (Wiley-Blackwell, 2018) pp. 195–216.
- <sup>54</sup>M. Xu, P. M. Felker, S. Mamone, A. J. Horsewill, S. Rols, R. J. Whitby, and Z. Bačić, "The Endofullerene HF@C60: Inelastic Neutron Scattering Spectra from Quantum Simulations and Experiment, Validity of the Selection Rule, and Symmetry Breaking," *J. Phys. Chem. Lett.* **10**, 5365–5371 (2019).
- <sup>55</sup>P. M. Felker and Z. Bačić, "Flexible water molecule in C60: Intramolecular vibrational frequencies and translation-rotation eigenstates from fully coupled nine-dimensional quantum calculations with small basis sets," *J. Chem. Phys.* **152**, 014108 (2020).
- <sup>56</sup>M. Xu, P. M. Felker, and Z. Bačić, "Light molecules inside the nanocavities of fullerenes and clathrate hydrates: Inelastic neutron scattering spectra and

- the unexpected selection rule from rigorous quantum simulations,” *Int. Rev. Phys. Chem.* **39**, 425–463 (2020).
- <sup>57</sup>D. E. Giblin, M. L. Gross, M. Saunders, H. Jimenez-Vazquez, and R. J. Cross, “Incorporation of Helium into Endohedral Complexes of C60 and C70 Containing Noble-Gas Atoms: A Tandem Mass Spectrometry Study,” *J Am Chem Soc* **119**, 9883–9890 (1997).
- <sup>58</sup>S. Rols, C. Bousige, J. Cambedouzou, P. Launois, J.-L. Sauvajol, H. Schober, V. Agafonov, V. Davydov, and J. Ollivier, “Unravelling low lying phonons and vibrations of carbon nanostructures: The contribution of inelastic and quasi-elastic neutron scattering,” *Eur. Phys. J. Spec. Top.* **213**, 77–102 (2012).
- <sup>59</sup>F. Cimpoesu, S. Ito, H. Shimotani, H. Takagi, and N. Dragoë, “Vibrational properties of noble gas endohedral fullerenes,” *Phys. Chem. Chem. Phys.* **13**, 9609–9615 (2011).
- <sup>60</sup>C. Cohen-Tannoudji, B. Diu, and F. Laloë, *Quantum Mechanics*, 2nd ed. (Wiley-VCH, 2020).
- <sup>61</sup>W. H. Shaffer, “Degenerate Modes of Vibration and Perturbations in Polyatomic Molecules,” *Rev. Mod. Phys.* **16**, 245–259 (1944).
- <sup>62</sup>S. Flügge, *Practical Quantum Mechanics*, Classics in Mathematics (Springer-Verlag, Berlin Heidelberg, 1999).
- <sup>63</sup>B. H. Bransden and C. J. Joachain, *Quantum Mechanics*, 2nd ed. (Pearson Prentice Hall, 2000).
- <sup>64</sup>H. A. Jiménez-Vázquez and R. J. Cross, “Equilibrium constants for noble-gas fullerene compounds,” *J. Chem. Phys.* **104**, 5589–5593 (1996).
- <sup>65</sup>L. Pang and F. Brisse, “Endohedral energies and translation of fullerene-noble gas clusters G@Cn (G = helium, neon, argon, krypton and xenon; n = 60 and 70),” *J. Phys. Chem.* **97**, 8562–8563 (1993).
- <sup>66</sup>F. Leclercq, P. Damay, M. Foukani, P. Chieux, M. C. Bellissent-Funel, A. Rassat, and C. Fabre, “Precise determination of the molecular geometry in fullerene C60 powder: A study of the structure factor by neutron scattering in a large momentum-transfer range,” *Phys. Rev. B* **48**, 2748–2758 (1993).
- <sup>67</sup>A. Terry Amos, T. Frank Palmer, A. Walters, and B. L. Burrows, “Atom—atom potential parameters for van der Waals complexes of aromatics and rare-gas atoms,” *Chemical Physics Letters* **172**, 503–508 (1990).
- <sup>68</sup>R. M. Parrish, L. A. Burns, D. G. Smith, A. C. Simmonett, A. E. De-Prince III, E. G. Hohenstein, U. Bozkaya, A. Y. Sokolov, R. Di Remigio, R. M. Richard, *et al.*, “Psi4 1.1: An open-source electronic structure program emphasizing automation, advanced libraries, and interoperability,” *Journal of chemical theory and computation* **13**, 3185–3197 (2017).
- <sup>69</sup>N. Mardirossian and M. Head-Gordon, “Thirty years of density functional theory in computational chemistry: an overview and extensive assessment of 200 density functionals,” *Molecular Physics* **115**, 2315–2372 (2017).
- <sup>70</sup>C. Lee, W. Yang, and R. G. Parr, “Development of the colle-salvetti correlation-energy formula into a functional of the electron density,” *Physical Review B* **37**, 785–789 (1988).
- <sup>71</sup>S. H. Vosko, L. Wilk, and M. Nusair, “Accurate spin-dependent electron liquid correlation energies for local spin density calculations: a critical analysis,” *Canadian Journal of Physics* **58**, 1200–1211 (1980).
- <sup>72</sup>A. D. Becke, “Density-functional thermochemistry. III. the role of exact exchange,” *The Journal of Chemical Physics* **98**, 5648–5652 (1993).
- <sup>73</sup>P. J. Stephens, F. J. Devlin, C. F. Chabalowski, and M. J. Frisch, “Ab initio calculation of vibrational absorption and circular dichroism spectra using density functional force fields,” *The Journal of Physical Chemistry* **98**, 11623–11627 (1994).
- <sup>74</sup>S. Grimme, S. Ehrlich, and L. Goerigk, “Effect of the damping function in dispersion corrected density functional theory,” *Journal of Computational Chemistry* **32**, 1456–1465 (2011).
- <sup>75</sup>S. Grimme, “Improved second-order møller–plesset perturbation theory by separate scaling of parallel-and antiparallel-spin pair correlation energies,” *The Journal of chemical physics* **118**, 9095–9102 (2003).
- <sup>76</sup>T. H. Dunning Jr, “Gaussian basis sets for use in correlated molecular calculations. i. the atoms boron through neon and hydrogen,” *The Journal of chemical physics* **90**, 1007–1023 (1989).
- <sup>77</sup>D. E. Woon and T. H. Dunning Jr, “Gaussian basis sets for use in correlated molecular calculations. iv. calculation of static electrical response properties,” *The Journal of chemical physics* **100**, 2975–2988 (1994).
- <sup>78</sup>N. Mardirossian and M. Head-Gordon, “ $\omega$ b97x-v: A 10-parameter, range-separated hybrid, generalized gradient approximation density functional with nonlocal correlation, designed by a survival-of-the-fittest strategy,” *Physical Chemistry Chemical Physics* **16**, 9904–9924 (2014).